Mechanical behaviour of brushite and hydroxyapatite coatings electrodeposited on newly developed FeMnSiPd alloys

J. Fornell[1]*, Y.P. Feng[1], E. Pellicer[1], S. Suriñach[1], M.D. Baró[1], J.Sort[1,2]

[1]*Departament de Física, Universitat Autònoma de Barcelona, E-08193 Bellaterra (Cerdanyola del Vallès), Spain*

[2]*ICREA, Pg. Lluís Companys 23, E-08010 Barcelona, Spain*

*Corresponding author. E-mail address: *Jordina.Fornell@uab.cat*

Keyworkds: Hydroxyapatite, calcium phospahte, iron, electrodeposition, nanoindentation.

Abstract

Calcium phosphate coatings (CaP) (i.e., brushite and hydroxyapatite) were grown by pulsed current electrodeposition on FeMnSiPd alloys, a newly developed material proposed for biomedical implants. The electrolytic baths contained $Ca(NO_3)_2 \cdot 4H_2O$ and $NH_4H_2PO_4$ as precursors. Bath additives, such as H_2O_2 and NaOH, were used to promote hydroxyapatite (HAp) coating formation directly from the bath. The effect of the electrodeposition parameters on the structure, morphology and mechanical performance of the coatings was investigated. Increasing the electrodeposition time from 900s to 3600s resulted in an increase of HAp over the dominant brushite structure. Addition of 2000 ppm of NaOH or 3000 ppm of H_2O_2 also promoted an increase of HAp fraction when compared to the coatings obtained from the additive-free bath. Nonetheless, pure HAp was only achieved with the addition of 4000 ppm of NaOH to the electrolyte. The morphologies of the CaP particles in the coatings ranged from needle- to plate-like structures depending on the electrodeposition parameters and the resulting phases. The mechanical behaviour of the coatings was studied by scratch testing and nanoindentation. As a general trend, the Young's modulus and hardness values of the electrodeposited coatings were lower than those reported for fully-dense HAp, independently of the deposition conditions, because of the porous morphology of the coatings. No signs of cracking or delamination were observed during nanoindentation

or scratch tests except for the coating prepared form the electrolyte containing 3000 ppm of H_2O_2.

1. Introduction

In recent years, there has been an increasing interest for new biodegradable metallic alloys that fulfil the requirements to be used as temporary medical implants. Up to date, Mg-based biodegradable metals (BMs) and their alloys have arisen as the most promising candidates to be used as BMs. They are free from toxic elements, exhibit fast biodegradability and a Young's modulus close to that of the human bone. However, the high amount of degradation products, H_2 evolution (and the subsequent formation of bubbles) and the high degradation rates of Mg may limit their use in certain applications where the implant needs to stay in the body for at least a specific period of time. Within this scenario, Fe-based alloys have gained increasing attention because of their mechanical properties, slower degradation rates and the good preliminary results obtained in *in-vitro* and *in-vivo* experiments [1,2]. For instance, recent studies showed that FeMn [3-9], FeMnPd [3,4], and FeMnSi [7] systems exhibit viable degradation rates and mechanical properties similar to those of 316L stainless steel. In particular, in our previous study on Fe-10Mn-6Si-1Pd alloy, a hardness value around 5.6 GPa and a reduced Young's modulus of 125 GPa were reported [8]. Concerning biocompatibility, the bulk alloy showed good initial cell adhesion. However, the pronounced ion release due to the formation of a cracked, loosely attached superficial oxide layer, hampered the cell proliferation on the surface of this alloy [8]. Nonetheless, no toxic effect has been observed due to local accumulation of Fe degradation products (i.e. $Fe(OH)_2$ $Fe(OH)_3$, Fe_2O_3 or $Fe(Mn)CO_3$) [9-11].

The development of ceramic coatings such as hydroxyapatite (HAp) or other various forms of calcium phosphates (CaP) on titanium and its alloys [12-15], stainless steel [16,17] and Mg-based alloys [18-20] has been documented to increase their biocompatibiliby [21-22]. This is possible since the bone can form direct chemical bonding to the bioactive CaP, without the occurrence of fibrous interface layers after implantation, which render poor mechanical stability between the implant and the bone. Moreover, in Mg-based alloys, where the main problem for their use as temporary implants are their exceedingly fast degradation

rates and the occurrence of high amounts of degradation products (such as Mg^{2+}, H_2 and OH^-), the growth of CaP coatings has proven to be an effective way to increase their corrosion resistance, hence retarding their degradability [18].

The most stable CaP phase in physiological environment (pH ≈ 7) is HAp. Other stable phosphates in acidic conditions are monetite ($CaHPO_4$), dicalcium phosphate dihidratate ($CaHPO_4 \cdot H_2O$) and octacalcium phosphate ($Ca_8(HPO_4)_2(PO_4)_4 \cdot 5H_2O$. These acidic CaP are thermodynamically unstable in physiological media, hence, they tend to transform into HAp once introduced in the body. In turn, the solubility of brushite is higher than that of HAp but, from a crystallographic point of view, HAp is more similar to natural bone tissue apatite [23]. Accordingly, hydroxyapatite shows excellent re-mineralization ability and bioactivity.

The methods used so far to deposit HAp onto metallic alloys include: plasma spraying [24], sputtering [25], pulsed laser-deposition [26], sol-gel [27], and electrochemical deposition [12-17]. Among them, electrodeposition turns out to be a suitable technique to grow uniform coatings with tuneable thickness and chemical composition on complex shaped structures at low temperature and relatively low processing costs. By adjusting the pH, the calcium to phosphorus ratio, the deposition temperature and additives content, the resulting degree of crystallinity, crystalline phases and the preferred orientation (texture), can be tailored. However, it has been reported that direct current electrodeposition usually results in loosely attached deposits to the substrate. To overcome this issue, pulsed electrodeposition has been established as a suitable alternative to grow well-adhered, high-quality HAp coatings [16-18].

While many studies focus on the synthetic strategies to obtain reliable CaP coatings by various methods, fewer efforts have been made to study the mechanical and adhesion properties of these coatings to the substrate. Nanoindentation is the most suitable technique to assess the mechanical properties and the adhesion of thin films. This technique has been recently applied to study the mechanical properties of CaP on stainless steel [28,29], magnesium alloys [30] and titanium [31-33]. However, to the best of our knowledge, there is no data available in the literature on the mechanical properties of CaP coatings grown by electrodeposition onto Fe-based alloys. The substrate type as well as the roughness of the coating may have an influence on the resulting mechanical performance of the studied

material. Hence, a detailed mechanical characterization is essential to understand and optimize the properties of Fe-based alloys coated with suitable bioactive materials. The aim of this work is thus to establish an efficient synthetic protocol to produce CaP coatings with good mechanical and adhesion properties on a newly developed Fe-10Mn-6Si-1Pd alloy.

2. Methods

Cylindrical rods of 3 mm in diameter and 3-4 cm in length with a nominal composition Fe-10Mn-6Si-1Pd (wt.%) were produced following the procedure described elsewhere [8]. Disks of 0.5 mm thickness were cut from the as-cat rod and used as substrates for the CaP deposition. In order to conveniently hold the substrates whilst providing electrical connection, metallic contacts were welded to the backside of the disks, which were subsequently embedded in cold resin. A polishing procedure with abrasive paper up to 4000 grit was then applied until a smooth metallic surface was exposed to view. The surface was ultrasonically cleaned for 5 min in ethanol prior to deposition. The CaP deposition was carried out in a single compartment, double-walled cell with a typical three-electrode configuration (connected to an Autolab 302N potentiostat/ galvanostat) (Figure 1a). A double junction Ag/AgCl with 3 M KCl inner solution and 1 M NaCl outer solution was used as reference electrode, while a Pt wire was used as counter-electrode. The electrolyte solution was prepared by mixing 0.042 mol/L of $Ca(NO_3)_2 \cdot 4H_2O$ and 0.025 mol/L of $NH_4H_2PO_4$ in Milli-Q water (pH = 4.05). In some cases, 3000 and 4000 ppm of H_2O_2 and 2000 and 4000 ppm of NaOH (reagent grade, ≥98%, pellets) were added to the electrolyte to favour HAp formation. The deposition was carried out at 65ºC under stirring. Pulsed current electrodeposition (Figure 1b) with a peak pulse current density of 0.75 mA/cm^2 and t_{ON} = 1s and t_{OFF} = 2s was implemented. The overall deposition time ranged from 900 s to 3600s. For comparison purposes, direct current (DC) electrodeposition was carried out at 0.75 mA/cm^2 for 1200s. To promote the brushite to HAp transformation, some specimens were rinsed in 0.1M NaOH solution for 72 h at room temperature.

Scanning electron microscopy (SEM) using a Zeiss Merlin microscope equipped with an energy dispersive X-ray (EDX) detector was used for morphological and compositional analyses. X-ray diffraction (XRD) was carried out using a Philips X'Pert diffractometer with Cu Kα radiation. The measurements were performed in the angular range 2θ = 10–60º with

a step size of 0.026º. To have further insight on the morphology and crystallographic structure of the coatings, transmission electron microscopy studies (TEM) were carried out in a JEOL JEM-2011 microscope operated at 200 kV.

To evaluate the thickness of the coatings deposited on the Fe-10Mn-6Si-1Pd substrates, a small part of the coating was removed from the substrate with a spatula or a non-sharp tweezer. Then, using the 3D Optical Surface Metrology System (DCM 3D) from Leica, which combines the confocal and interferometry technology, the height difference between the substrate and the coating was evaluated.

Nanoindentation and scratch experiments were performed using a Nanoindenter XP from MTS equipped with a Berkovich tip. The nanoindentation function consisted of a loading segment of 30 s, followed by a load holding segment of 10 s and an unloading segment of 30 s. The maximum applied load was set to 5 mN and 100 mN (two sets of experiments). The thermal drift was kept below ± 0.1 nm/s. From the load-displacement curves, the hardness and reduced Young's modulus values were derived using the method of Oliver and Pharr [34]. Note that nanoindentation can pose problems to assess the mechanical properties of porous films when the pores are very large and the applied load very small (so that the obtained results would then be dependent on whether a pore wall or a hole is indented, hence resulting in a pronounced scattering in the obtained data). However, the indents in our work embrace a large area of material and thus are representative of the overall mechanical response of the coating. In fact, nanoindentation has been rather widely used to assess the mechanical properties of porous materials. Typically the hardness and Young's modulus decrease with the porosity degree. This has been observed in diverse families of materials, such as metallic glasses [35], ceramics [36], crystalline metals and metallic alloys [37-39], silicon [40] or artificial porous rocks [41], measured from nanoindentation experiments and other techniques such as acoustic methods or macroscopic compression tests. Scratch tests were carried out applying an increasing normal load with the option for lateral force measurements. The normal load was linearly swept from 0 to 100 mN along the length of the scratch (500 μm) at a scratch velocity of 10 μm/s. The tests were repeated three times for each electrodeposition condition. Prior to scratch, an initial profile at 10 μN at the location where the scratch will be performed was carried out to assess the surface morphology. The

actual penetration depth of the indenter under the sample surface was estimated by comparing the indenter displacement normal to the surface during scratching with the topography of the original surface at each position along the scratch length. For the scratch segment, the roughness and the slope of the surface were considered in the calculation of the indenter penetration. After the scratch, in a similar manner, a final profile was recorded to establish the residual scratch depth.

3. Results and Discussion

3.1. Morphological and Structural characterization

Figure 2a shows the XRD patterns of the as-deposited coatings on Fe-10Mn-6Si-1Pd alloy at a pulsed current density of 0.75 mA/cm^2 for 900, 1800 and 3600 s from the electrolytic bath without additives. The XRD patterns reveal that the main phase of the as-deposited coatings, independently of the deposition time, is the dicalcium phosphate dihydratate (Brushite, $CaHPO_4 \cdot 2H_2O$) with minor content of hydroxyapatite (HAp, $Ca_{10}(PO_4)_6(OH)_2$). However, the peaks belonging to HAp gain intensity as the deposition time increases. The intensity ratio between the (020) peak belonging to brushite (at $2\theta = 11.70^o$) and the (002) peak belonging to HAp (at $2\theta = 25.9^o$) is listed in Table 1, as an indicative parameter for the predominant phase formation. The growth of HAp (and its predominance over brushite) can be explained by the chemical and electrochemical reactions that occur during the deposition process. The main reactions are listed below:

$$2H_2O + 2e^- = H_2 + 2OH^- \quad (1)$$

$$O_2 + 2H_2O + 4e^- = 4OH^- \quad (2)$$

$$2H_2PO_4^- + 2e^- = HPO_4^{2-} + H_2 \quad (3)$$

$$Ca^{2+} + HPO_4^{2-} + 2H_2O \rightarrow CaHPO_4 \cdot 2H_2O \quad (4)$$

It has been widely accepted that OH^-anions and H_2 gas bubbles are produced around the working electrode as a result of the reduction of oxygen and/or water (Eqs. 1 and 2), hence causing an increase of pH around the metal/solution interface [16]. However, at the beginning of the deposition process, the increase of pH is not enough to facilitate the formation of HAp, which is stable in the 9.5 to 12 pH range. On the contrary, brushite deposition is favored over

HAp as HPO_4^{2-}, which is reduced from $H_2PO_4^-$ (Eq. 3), combines with $Ca^{2+}$and H_2O to form $CaHPO_4 \cdot 2H_2O$ (Eq. 4), the kinetically stable CaP in acidic conditions. HPO_4^{2-} also reduces to yield PO_4^{3-} (Eq. 5); however, at the beginning of the electrodeposition process, the concentration of OH^- is not large enough to enable the formation of HAp [16].

$$2HPO_4^{2-} + 2e^- = 2PO_4^{3-} + H_2 \quad (5)$$

$$10Ca^{2+} + 6PO_4^{3-} + 2OH^- \rightarrow Ca_{10}(PO_4)_6(OH)_2 \quad (6)$$

Nonetheless, as deposition time increases, a decrease in the deposition potential is experimentally observed (from -0.68 V to -1.1 V) because of the formation and growth of the insulating CaP layer. This lower potential will result in the electrogeneration of a larger amount of OH^- ions, which will induce a local increase of the pH at the electrode interface, hence, favouring the growth of HAp (eq. 6). In fact, the increase of pH due to the formation of OH^- ions in the vicinity of the cathode induced by high cathode current densities (i.e. 2, 3, 10 mA/cm^2) has been extensively reported [16,17].

In order to accelerate the direct formation of HAp on Ti-, Mg-, and Fe-based alloys (i.e., with no need of additional thermal treatments) various approaches have been followed. For instance, some works reported that the addition of H_2O_2 into the electrolyte acts as an alternative electrochemical source of OH^- ions which can then promote the formation of HAp over other CaP species [16,42,43]. With this purpose, 3000 and 4000 ppm of H_2O_2 were added to the electrolyte. The addition of 3000 ppm of H_2O_2 results in an increase of the XRD peaks belonging to HAp although brushite is still present in the coating (Figure 2b). Increasing the amount of H_2O_2 to 4000 ppm does not further rise the HAp content (Table 1); furthermore, the surface of the alloy becomes partially covered by an orange layer attributed to oxides. The second approach to obtain pure HAp was to increase the pH of the electrolyte by the addition of NaOH. The addition of 2000 ppm of NaOH (pH = 5.05) results in a mixture of brushite and HAp phases, similar to the results obtained with 3000 ppm or 4000 ppm of H_2O_2 (Table 1). The addition of 4000 ppm of NaOH increases the pH of the electrolyte to 8.5. In this case, as it can be observed in the XRD pattern (Figure 2b), the coating only consists of HAp. Pure HAp is also obtained from an as-deposited mixture of brushite and

HAp by solution treatment in 0.1 M NaOH for 72 h at room temperature (Figure 2b). In this case, the chemical reaction for the brushite to HAp transformation is suggested to be:

$$10CaHPO_4 \cdot 2H_2O + 2OH^- \rightarrow Ca_{10}(PO_4)_6(OH)_2 + 20H_2O + 10H^+ + 4PO_4^{3-} \quad (7)$$

At first glance, the coatings produced by pulsed-current deposition are well adhered to the Fe-10Mn-6Si-1Pd substrate and the whole surface is homogeneously covered by HAp and/or brushite. However, the adhesion of the coatings grown by direct current deposition for 1200 s was not satisfactory and some parts peeled-off during handling, so no further characterization was carried out in this case. This fact has also been reported on other families of materials intended for biomedical applications such as Mg-based, Ti-based and stainless steel [16,18,44] and it is attributed to the concentration polarization formed during direct current electrodeposition because of the slow diffusion of the ions from the bulk solution to the cathode surface. The addition of a relaxation period allows the ions to diffuse closer to the cathode surface and, once the current is applied again, these ions will be deposited more effectively, hence enhancing the coating's adherence.

It is worth noticing that different morphologies can be observed depending on the resulting phases and deposition conditions. When the coating is formed by a mixture of brushite and HAp (i.e., the coatings produced without additives, with 3000 ppm of H_2O_2 or with 2000 ppm of NaOH), a morphology mainly consisting of thin rods or needles oriented perpendicularly or tilted with respect to the sample's surface can be observed (Figs. 3a and 3b). Some zones are covered with thicker disordered rods, particularly for shorter deposition times (i.e. 900 and 1800 s) (Fig. 3a). The EDX analysis corresponding to short deposition times (Fig. 3e), reveals that the ratio between Ca and P is approximately 1.05. This ratio is very close to the 1.0 ratio typically observed for stoichiometric brushite, thus indicating that the zones covered with thicker disordered threads mainly consist of brushite. Conversely, a larger Ca/P ratio of 1.25 (Fig. 3f) is detected in the zones consisting of thin threads (i.e., longer electrodeposition times). The increase of the Ca/P ratio can be indicative of HAp formation, probably on top of brushite. These observations are thus in agreement with the XRD results (Fig. 2a).

In turn, SEM imaging reveals that the coating produced from the electrolyte containing 4000 ppm of NaOH exhibits a plate-shaped morphology (Fig. 3c) characteristic of HAp formation.

The plates are hexagonal-shaped with preferred a (b)-axis orientation with an average size of ~2 μm. The Ca/P ratio, equal to 1.31 (Fig. 3g), is lower than the 1.67 value characteristic for the stoichiometric HAp, thus suggesting the formation of calcium-deficient HAp (CDHAp). Ca/P ratios between 1.31 and 1.67 were also observed by other authors and related these values to the chemical reactions occurring during the growth of the coatings [45,46]. The TEM image of this coating, shown in Fig. 4a, confirms the plate-like morphology typical of HAp. In agreement with the theoretical diffraction pattern of HAp (Ref. Code 00-011-0293), several interplanar distances can be calculated from the SAED pattern of Fig. 3b. For the sake of clarity, only the most intense diffraction spots/rings have been indexed in the figure.

Finally, the morphology observed in the solution treated (ST) coating after being immersed in 0.1M NaOH solution for 72 h (Fig. 3d) is similar to the morphology observed for as-deposited coatings for 900 and 1800 s. However, in this case the Ca/P ratio is closer to the theoretical value of 1.67, typical of stoichiometric HAp.

3.2.Mechanical Characterization

It is well-known that one of the drawbacks of CaP coatings prepared by DC electrodeposition is that their adherence to the underlying substrate is not sufficiently strong [16,18,44]. As a result, pulsed current electrodeposition has emerged as a more suitable technique to obtain well-adhered coatings. So far, the mechanical properties of CaP coatings (including HAp) produced by electrodeposition have not been studied in detail. Nanoindentation is a versatile technique that can be used to measure film adhesion; either from transverse scratching or by direct indentation [47]. Both approaches are used in this work to assess the mechanical properties of the coatings. Direct indentation is employed to evaluate the hardness, Young's modulus and plastic energy values of the CaP coatings and Fe-10Mn-6Si-1Pd substrate, while scratch tests are utilized to assess the adhesion of the layers to the substrate. Note that in this work a few CaP coatings were prepared by DC electrodeposition but their poor adhesion to the substrates resulted in peeling-off of some parts of the films during handling; henceforth, no further characterization was carried out. Only the coatings prepared by pulsed electrodeposition were investigated in detail by mechanical means.

3.2.1. Indentation tests

Indentation measurements (Fig. 5) were carried out for the coatings deposited for 3600 s from the additive-free bath (NA), from the bath containing 3000 ppm of H_2O_2 (curve denoted as H_2O_2), from the bath containing 4000 ppm g of NaOH (curve labelled as NaOH) and from the as-deposited coating produced from the additive-free electrolyte but subsequently solution treated with 0.1 M NaOH for 72 h (curve labelled as ST) to study the influence of the different phases and the synthetic parameters on the resulting mechanical properties. A summary of the mechanical properties is presented in Table 2. Nanoindentation is a suitable technique to measure the mechanical properties of thin films; however, to avoid unintentional influence from the properties of the substrate, it is commonly accepted that the maximum penetration depth should be lower than $1/10^{th}$ of the overall film thickness [47]. The indentation curves presented in Figure 5a and 5b were carried out using a maximum applied load of 5 mN and 100 mN, respectively. Notice that the maximum penetration depth exceeds the 10 % of the film thickness, even for P_{Max} = 5 mN (see Table 2). Thus, the Young's modulus and hardness values are influenced to some extent by the mechanical response of the substrate. Nonetheless, as can be observed in Table 2, the Young's modulus and hardness values of the substrate are much larger than those of the coatings, suggesting a limited contribution from the substrate. Therefore, the obtained values are still a good indicator of the dissimilar mechanical behaviour of the various coatings. Among the four different coatings tested in this work, the H_2O_2 one, which mainly consists of brushite and HAp, is the softest one, followed by the NA coating, which has a similar microstructure than the H_2O_2 one but has a lower HAp content. Several discontinuities can be observed from the load-displacement curve of the NaOH coating recorded up to a maximum applied load of 5 mN. These discontinuities are typically attributed to dislocation activity but, in this particular situation, they are likely due to cracking or bending of the HAp plates, as can be verified by imaging the nanoindentation imprint by SEM (Fig. 6a). The NaOH sample exhibits the largest hardness and Young's modulus values, which can be ascribed to the less porous nature of the coating as a result of the plated-shape morphology. In fact, the low Young's modulus and hardness values reported in this work (compared to the bulk values, i.e., H = 8.5 GPa and E_r = 130 GPa for bulk fully-dense HAp) [48] are mainly attributed to the particular morphology (i.e. plate-/needle-like) of the samples, which can be regarded as surface roughness or porosity [49].

In general, the mechanical properties of HAp coatings largely depend on the production technique. For instance, HAp films fabricated by plasma spraying using coarse powders exhibit a Young's modulus of 53-58 GPa [50], while those produced from a solution precursor exhibit a Young's modulus of 5-22 GPa [51]. In addition, He et al. [48] reported that the elastic modulus of fully-dense HAp produced by powder compaction and sintering process is ~130 GPa but it decreases to 20 GPa for a porosity level of 54%. Hence, differences in the elasticity of HAp coatings depend on the dissimilar microstructures that can be obtained using different synthetic pathways. In this work, when the applied load is 5 mN, the Young's modulus ranges from 4.5 to 15 GPa (depending on the microstructure and thickness of the coating). Larger Young's modulus values, from 19.5 to 67 GPa, are observed when the applied load is 100 mN. The same trend is observed for hardness; it increases with the maximum applied load. These trends can be attributed to a larger contribution from the substrate at larger applied loads but also to the densification of the coatings as the indenter penetrates into the material. SEM images of the imprints left behind on the NaOH coating after applying a maximum load of 5 mN and 100 mN are presented in Figure 6. No cracks or delamination can be observed at any condition, but a much higher compaction is evident when the applied maximum load is 100 mN.

Nanoindentation can also be used to assess the absorbed/dissipated energy by the specimens during the compressive tests, by comparing the values of the elastic and plastic indentation energies and their ratio. The area enclosed by the loading curve and the displacement axis corresponds to the total indentation energy (U_t). The area below the unloading part of the load-displacement curve and the displacement axis provides the elastic energy (U_e) recovered from the system during unloading. The area enclosed by the loading and unloading curves represents the unrecoverable inelastic or plastic energy ($U_{pl} = U_t - U_e$), related to the work spent during plastic deformation or other irreversible processes (e.g. cracking, crushing or compaction) and the energy stored in the form of residual stresses caused by the resultant impression [48]. The normalized inelastic energy (U_{pl}/U_t)*100 is commonly used as an indirect estimation of the energy absorbed by the material. From the nanoindentation curves presented in Figure 4 and from the (U_{pl}/U_t)*100 ratio in Table 2, it can be seen that the plastic energy is much higher than the elastic energy in all cases, which indicates the essentially plastic behaviour of the coatings. Namely, almost all the deformation caused by the applied

load in the coatings is irreversible. This is obviously related to the compaction process that takes places in these materials, as can be observed in Figure 6.

3.2.2. Scratch tests

Figure 7a shows the dependence of the penetration depth as a function of the scratch distance for the different investigated samples. A pronounced decrease of the penetration depth at the beginning of the scratch test is observed in all cases, followed by a less abrupt decrease at higher loads; this exponential decay can be attributed to the soft mechanical behaviour associated with the highly porous morphology and material densification at larger loads. However, some differences can be pointed out among the four samples. The H_2O_2 coating exhibits a larger penetration depth along the entire path. This is due to the larger porosity level associated with the needle-like morphology of this alloy and its consequently lower hardness (Table 2). In addition, the more abrupt penetration depth drops observed in this sample are also probably associated to the larger number of cracks stemming from the brittle morphology of the coating. Delamination or failure of the coating was not detected by post-scratch SEM imaging; however, a penetration of 15 μm and the sudden drops identified at 300 and 500 μm suggest a possible local failure. The SEM images of the last few microns of the scratches carried out in the H_2O_2 and NaOH coatings (see Fig. 8) reveal the local failure of the H_2O_2 coating. Conversely, only a densification phenomenon can be observed in the SEM image of the scratch performed in the NaOH coating. A maximum depth of ~9 μm is achieved in the NA coating, which is slightly larger than the ~5.5 μm maximum penetration depth for the ST and NaOH samples. At a scratch distance of ~150 μm the penetration does not further increase with the normal force as the densification process has finished and the penetration of the tip is much lower in the fully dense state. The dependence of friction force on the scratch distance is shown in Fig. 7b. The friction force increases linearly with the scratch distance. Larger frictional forces are observed for the NA, ST and H_2O_2 samples but much lower frictional forces, which will result in a lower friction coefficient, are detected for the NaOH coating.

4. Conclusions

Well-adhered CaP coatings on FeMnSiPd substrates have been successfully prepared by pulsed current electrodeposition. By tuning the deposition time and the composition of the bath, coatings with different amounts of brushite and HAp phases can be obtained. Electrodeposition of CaP results in needle-, rod- or plate-like morphologies leading to porous coatings. As a result, the measured Young's modulus and hardness are lower than those of fully-dense coatings with analogous compositions, hence approaching the values of both parameters in cortical bone. If the applied loads are high enough, the porous layers tend to be compacted, leading to an increase in both hardness and Young's modulus. Finally, delamination or failure of the coatings were not detected during scratch tests, thus corroborating the good adherence of the coatings to the Fe-based alloy.

Acknowledgements

This work has been partially funded by the 2014-SGR-1015 project from the Generalitat de Catalunya and the MAT2014-57960-C3-1-R from the Spanish Ministerio de Economía y Competitividad (MINECO) (co-financed by the Fondo Europeo de Desarrollo Regional, FEDER). Dr. Eva Pellicer is grateful to MINECO for the "Ramon y Cajal" contract (RYC-2012-10839). Dr. Jordina Fornell acknowledges the Juan de la Cierva Fellowship from MINECO (IJCI-2015-27030).

References

[1] R. Waksman, R. Pakala, R. Baffour, R. Seabron, D. Hellinga, F. O. Tio, Short-term effects of biocorrodible iron stents in porcine coronary arteries, J. Interv. Cardiol. 21 (2008) 15-20.

[2] M. Peuster, C. Hesse, T. Schloo, C. Fink, P. Beerbaum, C. von Schnakenburg, Long-term biocompatibility of a corrodible peripheral iron stent in the porcine descending aorta, Biomaterials 27 (2006) 4955-4962.

[3] M. Schinhammer, A. C. Hanzi, J. F. Loffler, P. J. Uggowitzer, Design strategy for biodegradable Fe-based alloys for medical applications, Acta Biomater. 6 (2010) 1705-1713.

[4] F. Moszner, A. S. Sologubenko, M. Schinhammer, C. Lerchbacher, A. C. Hanzi, H. Leitner, P. J. Uggowitzer, J. F. Loffler, Precipitation hardening of biodegradable Fe–Mn–Pd alloys, Acta Mater. 59 (2011) 981-991.

[5] M. Schinhammer, C. M. Pecnik, F. Rechberger, A. C. Hanzi, J. F. Loffler, P. J. Uggowitzer, Recrystallization behavior, microstructure evolution and mechanical properties of biodegradable Fe–Mn–C(–Pd) TWIP alloys, Acta Mater. 60 (2012) 2746-2756.

[6] H. Hermawan, D. Dube, D. Mantovani, Degradable metallic biomaterials: design and development of Fe-Mn alloys for stents, J. Biomed. Mater. Res. A 93 (2010) 1-11.

[7] B. Liu, Y. F. Zheng, L. Q. Ruan, In vitro investigation of Fe30Mn6Si shape memory alloy as potential biodegradable metallic material, Mater. Lett. 65 (2011) 540-543.

[8] Y.P. Feng, A. Blanquer, J. Fornell, H. Zhang, P. Solsona, M.D. Baró, S. Suriñach, E. Ibáñez, E. García-Lecina, X. Wei, R. Li, Ll. Barrios, E. Pellicer, C. Nogués, J. Sort, Novel Fe–Mn–Si–Pd alloys: insights into mechanical, magnetic, corrosion resistance and biocompatibility performances, J. Mater. Chem. B 4 (2016) 6402-6412.

[9] M. Moravej, A. Purnama, M. Fiset, J. Couet, D. Mantovani, Electroformed pure iron as a new biomaterial for degradable stents: degradation and preliminary cell viability studies, Acta Biomater. 6 (2010) 1843-1851.

[10] M. Peuster, P. Wohlsein, M. Brügmann, M. Ehlerding, K. Seidler, C. Fink, H. Brauer, A. Fischer, G. Hausdorf, A novel approach to temporary stenting: degradable cardiovascular stents produced from corrodible metal—results 6–18 months after implantation into New Zealand white rabbits, Heart 86 (2001) 563-569.

[11] P.P. Mueller, T. May, A. Perz, H. Hauser, M. Peuster, Control of smooth muscle cell proliferation by ferrous iron, Biomaterials 27 (2006) 2193-2200.

[12] K.A. Khor, C.S. Yip, P. Cheang, Ti- 6Al-4V/hydroxyapatite composite coatings prepared by thermal spray techniques, J. Therm. Spray Techn. 6 (1997) 109-115.

[13] A.K. Lynn, D.L. DuQuesnay, Hydroxyapatite-coated Ti–6Al–4V: Part 2: the effects of post-deposition heat treatment at low temperatures, Biomaterials 23 (2002) 1947-1953.

[14] E.A. dos Santos, M.S. Moldovan, L. Jacomine, M. Mateescu, J. Werckmann, K. Anselme, P. Mille, H. Pelletier, Oriented hydroxyapatite single crystals produced by the electrodeposition method, Mat. Sci. Eng. B 169 (2010) 138-144.

[15] M.H.P Da Silva, J.H.C. Lima, G.A. Soares, C.N. Elias, M.C. de Andrade, S.M. Best, I.R. Gibson, Bioactivity assessment of hydroxyapatite coatings produced by alkali conversion of monetite, Surf. Coat. Tech. 137 (2001) 270-276.

[16] D. Gopi, J. Indira, L. Kavitha, A comparative study on the direct and pulsed current electrodeposition of hydroxyapatite coatings on surgical grade stainless steel, Surf. Coat. Tech. 206, (2012) 2859-2869.

[17] G. Blanda, V. Brucato, F.C. Pavia, S. Greco, S. Piazza, C. Sunseri, R. Inguanta, Galvanic deposition and characterization of brushite/hydroxyapatite coatings on 316L stainless steel, Mat. Sci. Eng. C 64 (2016) 93-101.

[18] H.X. Wang, S.K. Guan, X. Wang, C.X. Ren, L.G. Wang, In vitro degradation and mechanical integrity of Mg–Zn–Ca alloy coated with Ca-deficient hydroxyapatite by the pulse electrodeposition process, Acta Biomater. 6 (2010) 1743-1748.

[19] Y.W. Song, D.Y. Shan, E.H. Han, Electrodeposition of hydroxyapatite coating on AZ91D magnesium alloy for biomaterial application, Mater. Lett. 62 (2008) 3276.

[20] H.M. Mousa, A.P. Tiwari, J. Kim, S.P. Adhikari, C.H. Park, C.S. Kim, A novel in situ deposition of hydroxyapatite nanoplates using anodization/hydrothermal process onto magnesium alloy surface towards third generation biomaterials, Mater. Lett. 164 (2016) 144-147.

[21] M.H.P. Da Silva, G.A. Soares, C.N. Elias, I.R. Gibson, S.M. Best, Transformation of monetite to hydroxyapatite in bioactive coatings on titanium, Key Eng. Mater. 192 (2000) 159-162.

[22] R. Rohanizadeh, R.Z. LeGeros, M. Harsono, A. Bendavid, Adherent apatite coating on titanium substrate using chemical deposition, J. Biomed. Mater. Res. A 72 (2005) 428-438.

[23] E. Fernándze, F.J. Gil, M.P. Ginebra, F.C.M. Driessens, J.A. Planell, S.M. Best, Calcium phosphate bone cements for clinical applications – part I: solution chemistry, J. Mater. Sci. Mater. Med. 10 (1999) 169-176.

[24] H. Wang, N. Eliaz, Z. Xiang, H.P. Hsu, M. Spector, L.W. Hobbs, Early bone apposition in vivo on plasma-sprayed and electrochemically deposited hydroxyapatite coatings on titanium alloy, Biomaterials 27 (2006) 4192-4203.

[25] Y. Yang, K.H. Kim, J.L Ong, A review on calcium phosphate coatings produced using a sputtering process—an alternative to plasma spraying, Biomaterials 26 (2005) 327-337.

[26] Y. Suda, H. Kawasaki, T. Ohshima, S. Nakashima, S. Kawazoe, T. Toma, Hydroxyapatite coatings on titanium dioxide thin films prepared by pulsed laser deposition method, Thin Solid Films 506 (2006) 115-119.

[27] Y.L. Jeyachandran, S. Venkatachalam, B. Karunagaran, Sa.K. Narayandass, D. Mangalaraj, C.Y. Bao, C.L. Zhang, Bacterial adhesion studies on titanium, titanium nitride and modified hydroxyapatite thin films, Mat. Sci. Eng. C 27 (2007) 35-41.

[28] D. Sidane, D. Chicot, S. Yala, S. Ziani, H. Khireddine, A. Iost, X. Decoopman, Study of the mechanical behavior and corrosion resistance of hydroxyapatite sol-gel thin coatings on 316L stainless steel pre-coated with titania film, Thin Solid Films 593 (2015) 71-80.

[29] Mina, A. Castaño, J.C. Caicedo, H.H. Caicedo, Y. Aguilar, Determination of physical properties for β-TCP + chitosan biomaterial obtained on metallic 316L substrates, Mater. Chem. Phys. 160 (2015) 296-307.

[30] M.A. Surmeneva, A.I. Tyurin, T.M. Mukhametkaliyev, T.S. Pirozhkova, I.A. Shuvarin, M.S. Syrtanov, R.A. Surmenev, Enhancement of the mechanical properties of AZ31 magnesium alloy via nanostructured hydroxyapatite thin films fabricated via radio-frequency magnetron sputtering, J. Mech. Behav. Biomed. 46 (2015) 127-136.

[31] H.Wang, C.J. Lin, R. Hu, F. Zhang, L.W. Lin, A novel nano-micro structured octacalcium phosphate/ protein composite coating on titanium by using an electrochemically induced deposition, J. Biomed. Mater. Res. A 87 (2008) 698-705.

[32] X. Bai, S. Sandukas, M. R. Appleford, J.L. Ong, A. Rabiei, Deposition and investigation of functionally graded calcium phosphate coatings on titanium, Acta Biomater. 5 (2009) 3563-3572.

[33] R. Drevet, N. Ben Jaber, J. Fauré, A. Tara, A. Ben Cheikh Larbi, H. Benhayoune, Electrophoretic deposition (EPD) of nano-hydroxyapatite coatings with improved mechanical properties on prosthetic Ti6Al4V substrates, Surf. Coat. Tech. 301, (2016) 94-99.

[34] W.C. Oliver, G.M. Pharr, An improved technique for determining hardness and elastic modulus using load and displacement senseing indentation experiments, J. Mater. Res. 7 (1992) 1564-1583.

[35] G. Xie, M. Fukuhara, D.V. Louzguine-Luzgin and A. Inoue, Ultrasonic characteristics of porous Zr55Cu30Al10Ni5 bulk metallic glass fabricated by spark plasma sintering, Intermetallics, 18 (2010) 2014-2018.

[36] F. Tancret and F. Osterstock, Indentation behaviour of porous materials: Application to the Vickers indentation cracking of ceramics, Phil. Mag., 83 (2003) 125-136.

[37] D.T. Queheillalt, Y. Katsumura and H.N.G. Wadley, Synthesis of stochastic open cell Ni-based foams, Scripta Mater., 50 (2004) 313-317.

[38] J. Biener, A.M. Hodge, A.V. Hamza, L.M. Hsiung and J.H. Satcher, Nanoporous Au: A high yield strength material, J. Appl. Phys., 97 (2005) 024301.

[39] J.C. Lin, Y.S. Chen, C.F. Huang, J.H. Yang, T.K. Chang, C.-L. Wu, Y.R. Hwang and T.C. Chen, Mechanical properties of copper micrometer pillars fabricated by intermittent MAGE process, Int. J. Electrochem. Sci., 6 (2011) 3536-3549.

[40] D. Bellet, P. Lamagnère, A. Vincent and Y. Bréchet, Nanoindentation investigation of the Young's modulus of porous silicon, J. Appl. Phys., 80 (1996) 3772-3776.

[41] M.H. Leite and F. Ferland, Determination of unconfined compressive strength and Young's modulus of porous materials by indentation tests, Engng. Geol., 59 (2001) 267-280.

[42] R. Drevet, H. Benhayoune, L. Wortham, S. Potiron, J. Douglade, D. Laurent-Maquin, Effects of pulsed current and H2O2 amount on the composition of electrodeposited calcium phosphate coatings, Mater. Charact. 61 (2010) 786-795.

[43] D.T.M. Thanh, P.T. Nam, N.T. Phuong, L.X. Que, N. Van Anh, T. Hoang, T.D. Lam, Controlling the electrodeposition, morphology and structure of hydroxyapatite coating on 316L stainless steel, Mat. Sci. Eng. C 33 (2013) 2037-2045.

[44] D.J. Blackwood, K.H.W. Seah, Galvanostatic pulse deposition of hydroxyapatite for adhesion to titanium for biomedical purposes, Mater. Sci. Eng. C 30 (2010) 561-565.

[45] N. Ohtsu, S. Hiromoto, M. Yamane, K. Satoh, M. Tomozawa, Chemical and crystallographic characterizations of hydroxyapatite- and octacalcium phosphate-coatings on magnesium synthesized by chemical solution deposition using XPS and XRD, Surf. Coat. Tech. 218 (2013) 114-118.

[46] R.M. Wilson, J.C. Elliott, S.E.P. Dowker, L.M. Rodriguez-Lorenzo, Rietveld refinements and spectroscopic studies of the structure of Ca-deficient apatite, Biomaterials 26 (2005) 1317-1327.

[47] A.C. Fischer-Cripps. Nanoindentation, Springer, New York, 2002.

[48] L.H. He, O.C. Standard, T. T.Y. Huang, B.A. Latella, M.V. Swain, Mechanical behaviour of porous hydroxyapatite, Acta Biomater. 4 (2008) 577-586.

[49] D. Esqué-de los Ojos, J. Zhang, J. Fornell, E. Pellicer, J. Sort, Nanomechanical behaviour of open-cell nanoporous metals: Homogeneous versus thickness-dependent porosity, Mech. Mater. 100 (2016) 167-174.

[50] L. Fu, K.A. Khor, J.P. Lim, Processing, microstructure and mechanical properties of yttria stabilized zirconia reinforced hydroxyapatite coatings, Mater. Sci. Eng. A 316 (2001) 46-51.

[51] A. Mejias, R.T. Candidato Jr., L. Pawłowski, D. Chicot, Mechanical properties by instrumented indentation of solution precursor plasma sprayed hydroxyapatite coatings: Analysis of microstructural effect, Surf. Coat. Tech. 298 (2016) 93-102.

Figure and Table Captions

Fig. 1: (a) Scheme of the three-electrode configuration used to synthesize the CaP coatings. (b) Current-time waveform used for pulse plating electrodeposition.

Fig. 2: X-ray diffraction patterns of pulse-plated coatings on Fe-10Mn-6Si-1Pd alloys produced from: (a) the additive-free bath (no additives, NA curve) for 900 s, 1800 s and 3600 s, (b) the bath containing 3000 ppm of H_2O_2 (H_2O_2 curve) for 3600 s, the bath containing 4000 ppm of NaOH (NaOH curve) for 3600 s, and the additive-free bath for 3600 s followed by solution treatment (ST curve) with 0.1 M NaOH for 72 h.

Fig. 3: SEM images of coatings produced from: (a) the additive-free bath for 1800 s, (b) the additive-free bath for 3600 s, (c) the bath containing 4000 ppm of NaOH for 3600 s and (d) the additive-free bath for 3600 s and solution treated with 0.1 M NaOH for 72 h. The insets are higher magnifications SEM images. (e), (f), (g) and (h) are the EDX spectra corresponding to the areas depicted in (a), (b), (c) and (d), respectively.

Fig. 4: (a) TEM image of the coating produced from the bath containing 4000 ppm of NaOH for 3600 s, (b) corresponding SAED pattern.

Fig. 5: Load-displacement curves of the coated-Fe-10Mn-6Si-1Pd alloys applying a maximum load of (a) 5 mN and (b) 100 mN. NA stands for the coating obtained from the additive-free bath, H_2O_2 stands for the coating obtained from H_2O_2 containing electrolyte, NaOH applies to the coating produced from NaOH containing electrolyte and ST refers to the coating obtained from the additive-free bath further treated with NaOH at RT for 72 h.

Fig. 6: SEM images of the indentation imprints left on the coating produced from the bath containing 4000 ppm of NaOH at a maximum applied load of (a) 5 mN (b) 100 mN.

Fig. 7: Scratch tests carried out on the coated-Fe-10Mn-6Si-1Pd alloys showing (a) penetration depth *versus* scratch distance, (b) friction force *versus* scratch distance. The same nomenclature as in Figure 4 is used.

Fig. 8: SEM images of the last few microns of the scratch tests performed on the coatings produced from (a) NaOH containing electrolyte and (b) H_2O_2 containing electrolyte coating.

Table 1: Ratio between the experimental intensities of the (020) peak from brushite and the (002) peak from HAp.

Table 2: Thickness and mechanical properties of the coatings and the Fe-10Mn-6Si-1Pd substrate measured by nanoindentation applying maximum forces (P_{Max}) of 5mN and 100 mN. H, E_r, U_{pl} and U_t denote the hardness, reduced Young's modulus, plastic indentation energy and total indentation energy, respectively.

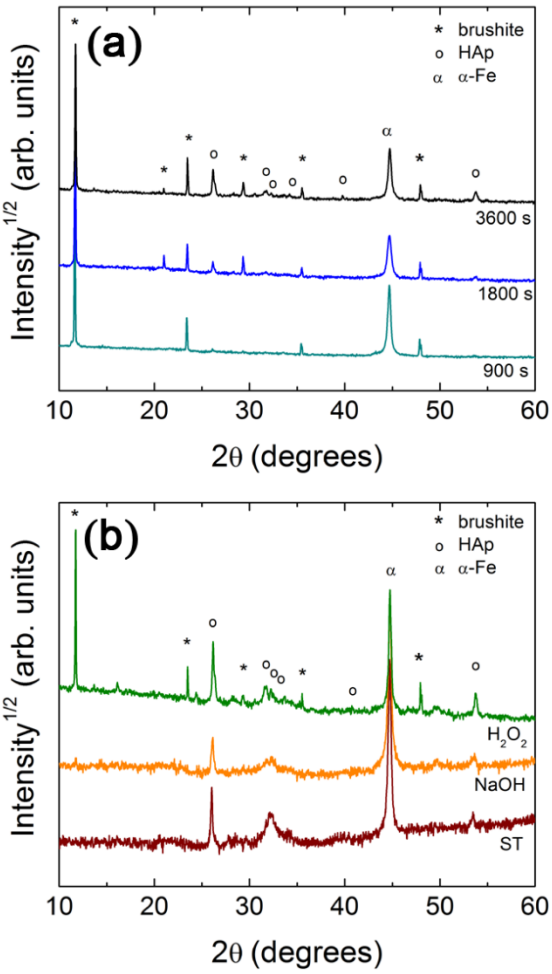

Fig. 1: X-ray diffraction patterns of pulse-plated coatings on Fe-10Mn-6Si-1Pd alloys produced from: (a) the additive-free bath (no additives, NA curve) for 900 s, 1800 s and 3600 s, (b) the bath containing 3000 ppm of H_2O_2 (H_2O_2 curve) for 3600 s , the bath containing 0.2 g of NaOH (NaOH curve) for 3600 s, and the additive-free bath for 3600 s followed by solution treatment (ST curve) with 0.1 M NaOH for 72 h.

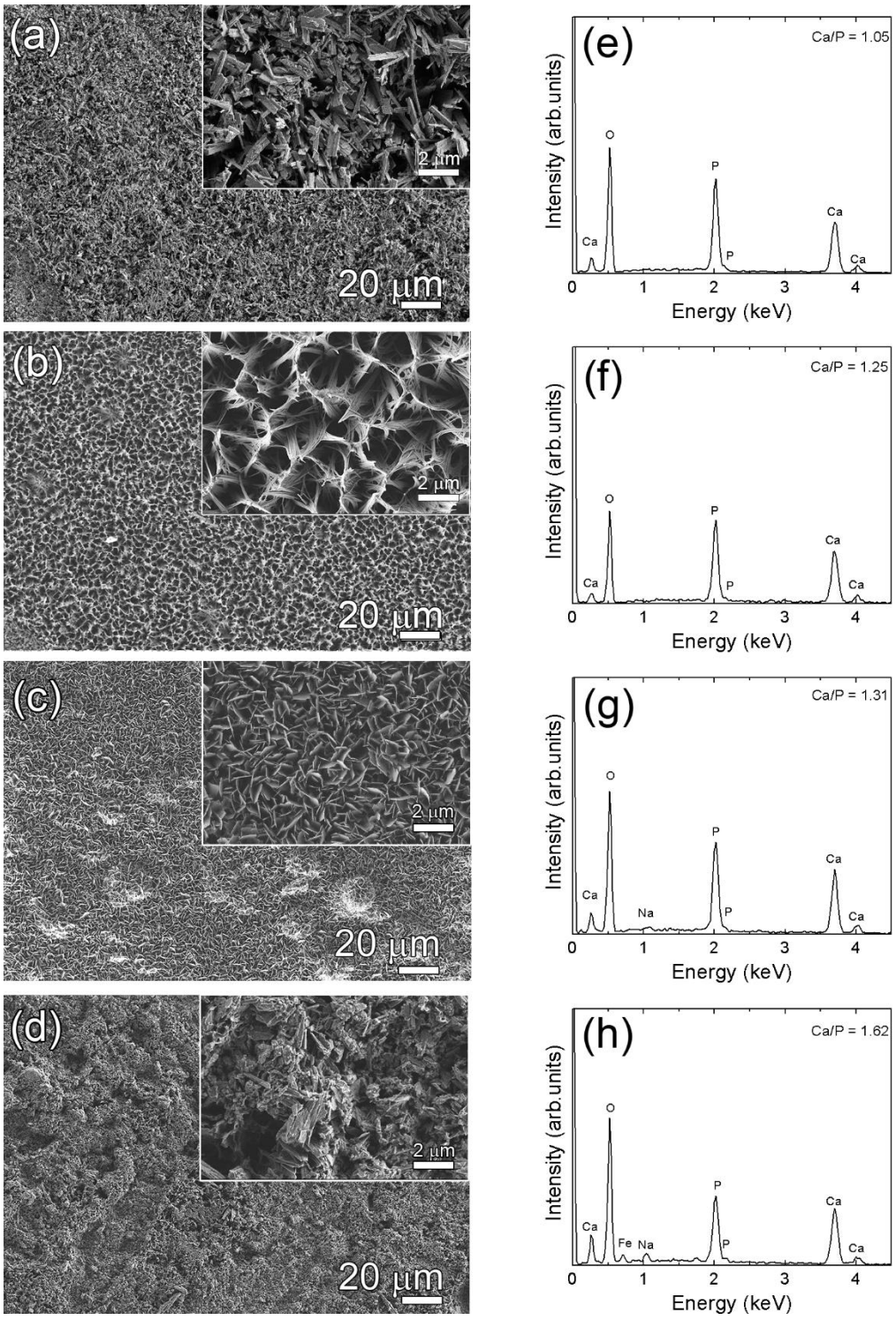

Fig. 2: SEM images of coatings produced from: (a) the additive-free bath for 1800 s, (b) the additive-free bath for 3600 s, (c) the bath containing 0.2 g of NaOH for 3600 s and (d) the additive-free bath for 3600 s and solution treated with 0.1 M NaOH for 72 h. The insets are higher magnifications SEM images. (e), (f), (g) and (h) are the EDX spectra corresponding to the areas depicted in (a), (b), (c) and (d), respectively.

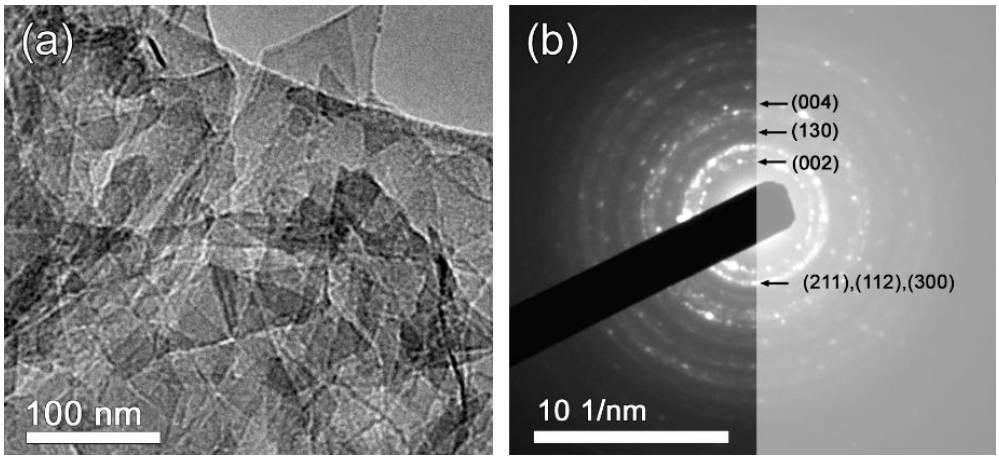

Fig. 3: (a) TEM image of the coating produced from the bath containing 0.2 g of NaOH for 3600 s, (b) corresponding SAED pattern.

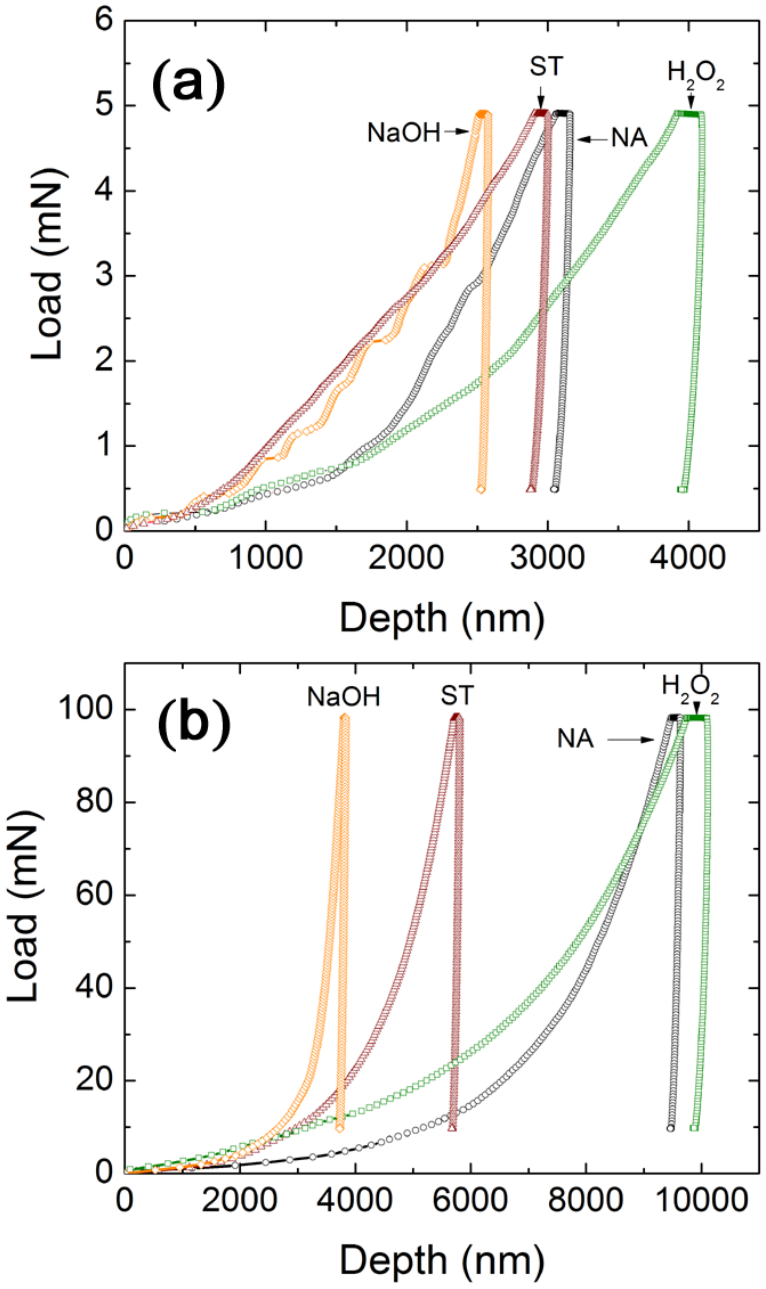

Fig. 4: Load-displacement curves of the coated-Fe-10Mn-6Si-1Pd alloys applying a maximum load of (a) 5 mN and (b) 100 mN. NA stands for the coating obtained from the additive-free bath, H_2O_2 stands for the coating obtained from H_2O_2 containing electrolyte, NaOH applies to the coating produced from NaOH containing electrolyte and ST refers to the coating obtained from the additive-free bath further treated with NaOH at RT for 72 h.

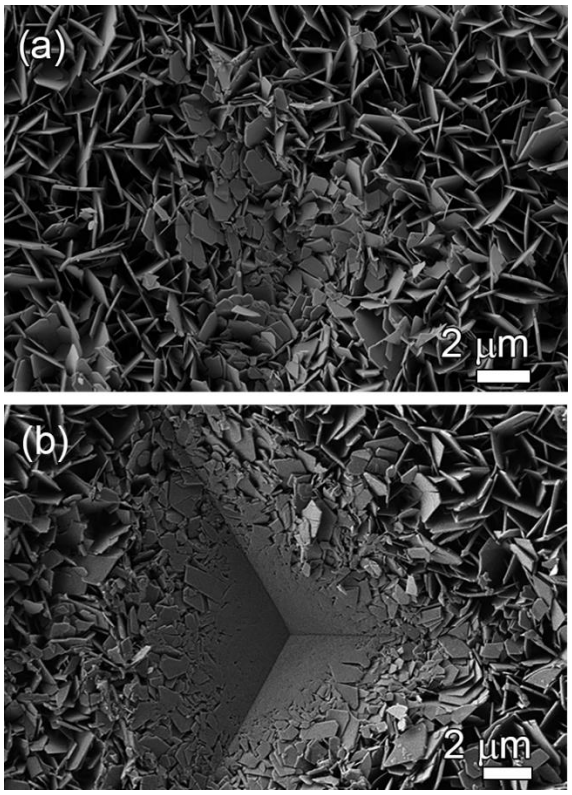

Fig. 5: SEM images of the indentation imprints left on the coating produced from the bath containing 0.2 g of NaOH at a maximum applied load of (a) 5 mN (b) 100 mN.

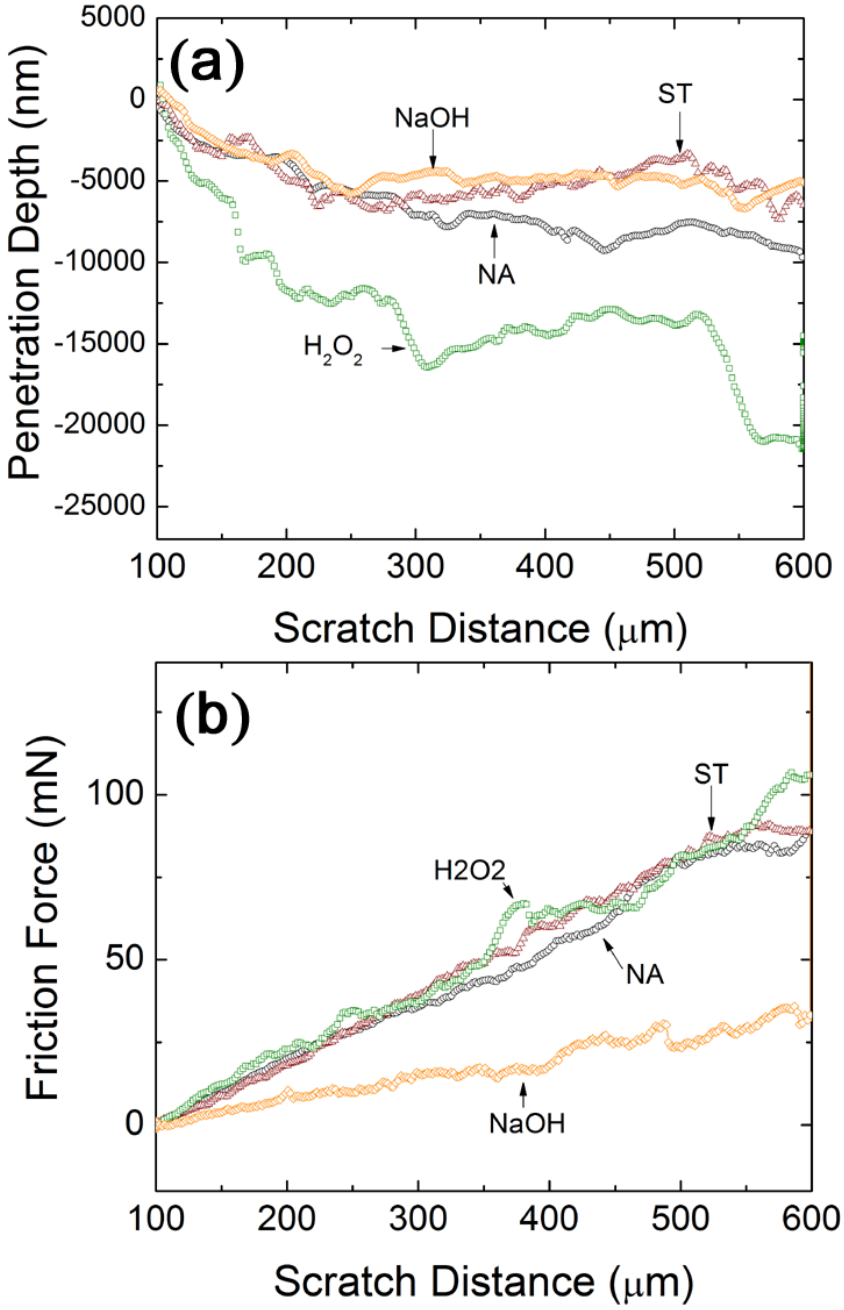

Fig. 6: Scratch tests carried out on the coated-Fe-10Mn-6Si-1Pd alloys showing (a) penetration depth *versus* scratch distance, (b) friction force *versus* scratch distance. The same nomenclature as in Figure 4 is used.

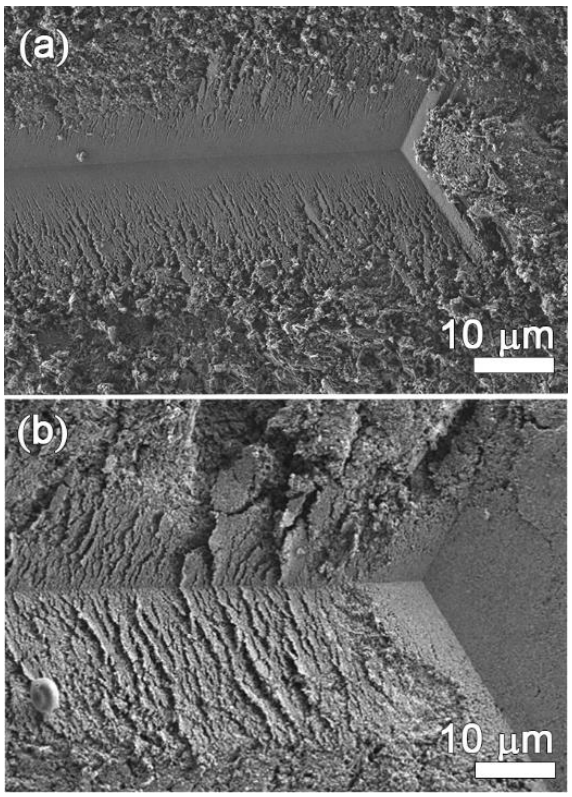

Fig. 7: SEM images of the last few microns of the scratch tests performed on the coatings produced from (a) NaOH containing electrolyte and (b) H_2O_2 containing electrolyte coating.

Additives	time	$I_{Brushite\ (020)\ peak}/I_{HAp\ (002)\ peak}$
-	900	141
-	1800	36.6
-	3600	23
3000 ppm H_2O_2	3600	1.11
4000 ppm H_2O_2	3600	3.86
0.1 g NaOH	3600	15

Table 1: Ratio between the experimental intensities of the (020) peak from brushite and the (002) peak from HAp.

Sample	Thickness (μm)	P_{max} (mN)	H (GPa)	E_r (GPa)	U_{pl}/U_t*100
Fe-30Mn-6Si-1Pd substrate	2000-3000	5	8.6 ± 0.6	226 ± 15.0	76.0 ± 2.5
		100	5.6 ± 0.4	193 ± 5	82 ± 4
NA	13.4 ± 0.9	5	0.021 ± 0.015	4.5 ± 1.4	95 ± 3
		100	0.050 ± 0.011	21 ± 5	96.5 ± 0.5
H_2O_2	14.4 ± 1.4	5	0.014 ± 0.004	3.1 ± 1.0	97.1 ± 0.9
		100	0.047 ± 0.016	20 ± 6	97.9 ± 0.4
0.2 g NaOH	12.8 ± 0.5	5	0.031 ± 0.009	15 ± 4	97.3 ± 0.3
		100	0.31 ± 0.12	67 ± 9	89.2 ± 1.9
ST	3.3 ± 0.8	5	0.024 ± 0.009	4.7 ± 1.2	95.8 ± 0.7
		100	0.15 ± 0.04	45 ± 7	96.1 ± 1.8

Table 2: Thickness and mechanical properties of the coatings and the Fe-10Mn-6Si-1Pd substrate measured by nanoindentation applying maximum forces (P_{Max}) of 5mN and 100 mN. H, E_r, U_{pl} and U_t denote the hardness, reduced Young's modulus, plastic indentation energy and total indentation energy, respectively.